Research Square

Preprints are preliminary reports that have not undergone peer review.
They should not be considered conclusive, used to inform clinical practice,
or referenced by the media as validated information.

Molecular basis for allosteric regulation of RyR1 channel gating: effects of a therapeutic drug and oxidation-mimicking mutation

Karissa Sanbonmatsu

kys@lanl.gov

Los Alamos National Laboratory https://orcid.org/0000-0002-7965-7392

Jigneshkumar Prajapati

Birla Institute of Technology (BITS) Pilani

Marco Miotto

Columbia University Vagelos College of Physicians and Surgeons https://orcid.org/0000-0001-8851-4863

Jeevan GC

AbbVie

Haikel Dridi

Columbia University https://orcid.org/0000-0001-9533-7367

Qi Yuan

Columbia University

Anetta Wronska

Columbia University https://orcid.org/0000-0003-2288-2596

Yang Liu

Columbia University Vagelos College of Physicians and Surgeons https://orcid.org/0000-0002-8343-4431

Zephan Melville

Columbia University Vagelos College of Physicians and Surgeons

Andrew Marks

Columbia University https://orcid.org/0000-0002-4316-5775

Joachim Frank

Columbia University https://orcid.org/0000-0001-5449-6943

Article

Keywords:

Posted Date: November 3rd, 2026

DOI: https://doi.org/10.21203/rs.3.rs-9535852/v1

License: This work is licensed under a Creative Commons Attribution 4.0 International License.
Read Full License

Additional Declarations: Yes there is potential Competing Interest. A.R.M. owns stock in RyCarma Therapeutics Inc., a company developing compounds targeting RyR.

Molecular basis for allosteric regulation of RyR1 channel gating: effects of a therapeutic drug and oxidation-mimicking mutation

Jigneshkumar Dahyabhai Prajapati,[1,2,3†] Marco C Miotto[4†], Jeevan GC[5†], Haikel Dridi[4], Qi Yuan[4], Anetta Wronska[4], Yang Liu[4], Zephan Melville[4], Andrew Marks[4*], Joachim Frank[5,6*], Karissa Y. Sanbonmatsu[1,2*#]

[1]Theoretical Biology and Biophysics, Los Alamos National Laboratory, Los Alamos, New Mexico 87545, USA

[2]New Mexico Consortium, Los Alamos, New Mexico 87544, USA

[3]Department of Biological Sciences, Birla Institute of Technology and Science (BITS) Pilani, Pilani, Rajasthan, India

[4]Department of Physiology and Cellular Biophysics, Columbia University Vagelos College of Physicians and Surgeons, New York, NY 10032, USA

[5]Department of Biochemistry and Molecular Biophysics, Columbia University, New York, NY, USA

[6]Department of Biological Sciences, Columbia University, New York, NY, USA

[†]First authors

*Corresponding authors

[#]To whom correspondence may be addressed. Email: kys@lanl.gov

Abstract

RyR1, an enormous, approximately 2.2 MDa, tetrameric calcium-release channel in the sarcoplasmic reticulum (SR) of skeletal muscle, is essential for excitation-contraction coupling. Pathogenic mutations in RyR1 cause RyR1-related myopathies. ARM210 (S48168), a Rycal-class drug, has shown promise in treating RyR1-related myopathies in a recently concluded phase 1b clinical trial. Structural studies revealed that ARM210 binds to the peripheral RY1&2 domain of RyR1, stabilizing it in a closed state to prevent aberrant SR Ca^{2+} leak. Here, we investigate ARM210's mechanism of action at the atomistic level using extensive all-atom (~2.5 million atoms) explicit-solvent molecular dynamics simulations totaling 36.6 μs. Simulations revealed a long-range allosteric pathway in the wild-type RyR1 that propagates over 200 Å, linking the RY1&2 domain to the pore-forming S6 helices of adjacent protomers and enabling pore opening. Subsequently, we demonstrated that ARM210 binding stabilizes the RY1&2 domain in a closed conformation, rigidifying the cytosolic shell and activation core and disrupting the allosteric network necessary for pore dilation. These findings describe a plausible mode of action for how ARM210 stabilizes RyR1 in a closed state by modulating long-range allostery. Furthermore, we show that this allosteric regulatory network is perturbed by the oxidative stress-mimicking C3892D mutation near the Ca^{2+} activator site, identified via mass spectrometry, live-cell fluorescence microscopy, and electrophysiology.

Introduction

Ryanodine receptors (RyRs), situated in the sarco-/endoplasmic reticulum (SR/ER) membrane release calcium (Ca^{2+}) ions during excitation-contraction coupling in skeletal and cardiac muscle[1–4]. RyR1 is mainly a skeletal isoform, while RyR2 and RyR3 are cardiac and brain-associated isoforms, respectively, though all appear in multiple cell types.[5]. In skeletal muscle, the dihydropyridine receptors (DHPRs), $Ca_v1.1$ voltage-gated Ca^{2+} channels, in the T-tubule membrane sense membrane potential changes and undergo conformational changes, which subsequently via a mechanical coupling activate the RyR1 channels[6]. Half of the RyR1 channels interact with clusters of four DHPRs, while the remaining half of RyR1 channels situated between these clusters are activated through a mechanism known as coupled gating, independent of DHPRs association[7–10]. RyR2 is activated by the influx of Ca^{2+} through a $Ca_V1.2$ triggering a mechanism termed Ca^{2+}-induced Ca^{2+}-release (CICR)[11].

RyR activation and the subsequent downstream Ca^{2+} signaling are regulated by various ligands and protein interactions. Small molecules, ATP, Ca^{2+}, and caffeine are key activators (cofactors) which play an agonistic role in pore opening, whereas the plant alkaloid ryanodine serves as a specific RyR channel modulator locking the channel in a half-open state at low concentrations and blocking it at high concentrations[12,13]. RyRs interact with several other transmembrane proteins, such as triadin and junctin, and soluble proteins, including calmodulin, calstabin, calsequestrin, phosphatases and kinases[14–16]. RyR1 binds calmodulin-1 (Cm1), which activates the channel at low cytosolic Ca^{2+} concentrations (< 1 μM) but inhibits it at elevated levels (> 1 mM) following intracellular Ca^{2+} release[17]. Calstabin-1 (FKBP12) interacts with RyR1, while its homolog calstabin-2 (FKBP12.6) binds RyR2; both stabilize the closed state, regulate coupled gating between neighboring RyRs, and modulate the pore opening[18,19]. Calstabins dissociate from RyR channels under pathological conditions such as inherited myopathies, and heart failure, and aging where post-translational modifications of RyRs (e.g., phosphorylation, oxidization) increase their off-rate [20–22]. This leads to SR Ca^{2+} leak into the cytosol and aberrant downstream Ca^{2+} signaling[23,24], and has been linked to muscular dystrophy[25], myopathies[26], heart failure[21,23,27–29], diabetes[30], Huntington's disease[31], and Alzheimer's disease[32]. To counteract this, benzothiazepine derivatives termed Rycals were developed to stabilize RyRs and prevent Ca^{2+} leaks. Recently, the ARM210 (S48168) molecule, a Rycal, showed safety, tolerability, and possible efficacy in a phase 1b clinical trial (120 and 200 mg daily for 28 days)

in adults with RYR1-related myopathy[33]. This drug has also shown potential to repair leaky RyR2 channels, and a phase 2 clinical trial for heart failure is being planned[34].

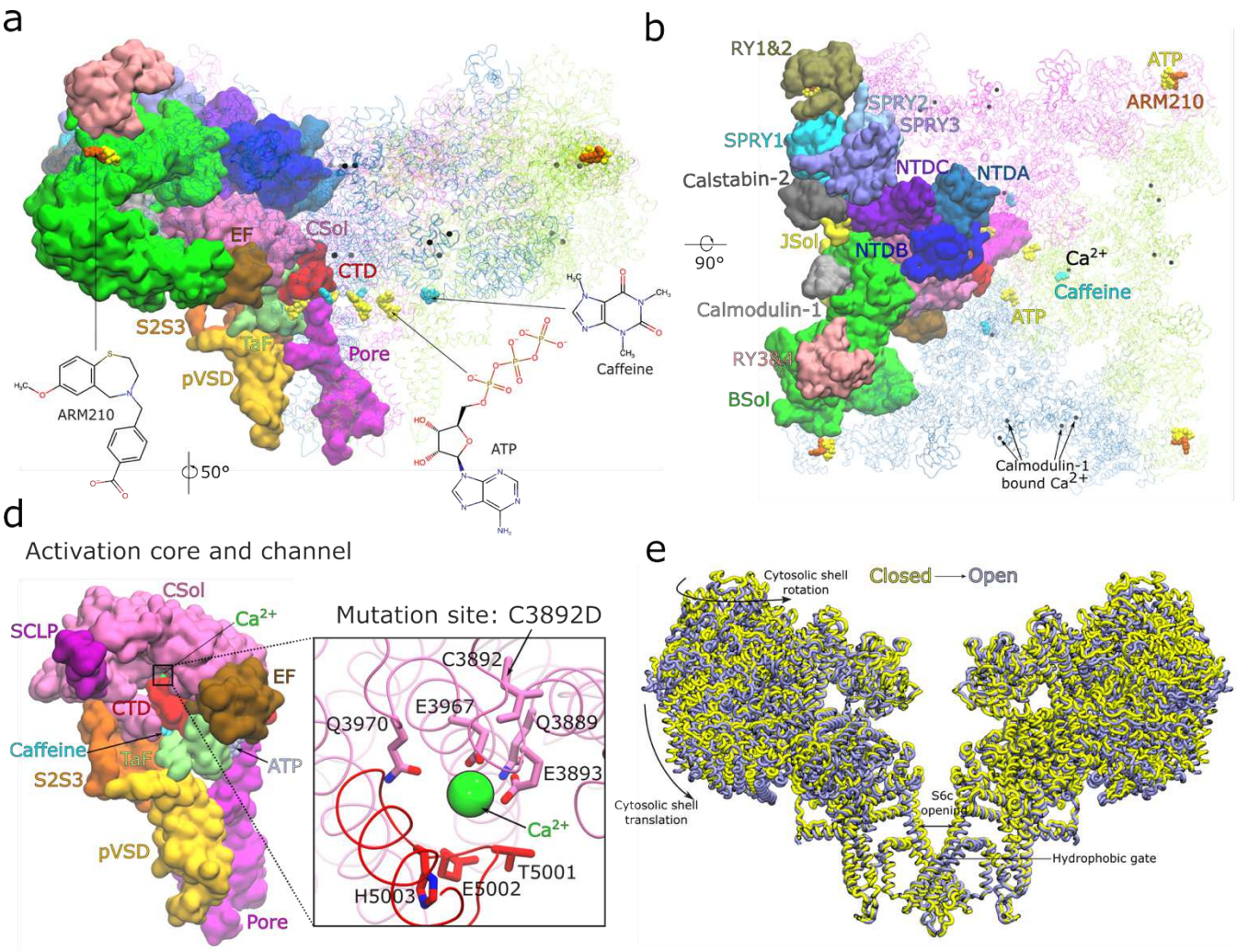


Figure 1: Structural features of the RyR1 channel. a) Side view and b) top view of tetrameric RyR1, with one protomer shown in surface and the others in cartoon representation. The 19 domains of RyR1, together with the associated proteins calmodulin-1 and calstabin-1, are color-coded. Three cofactors, ATP, caffeine, and Ca^{2+}, occupy the activation core, while the Rycal ARM210 drug, cooperatively bound with ATP, is located in the RY1&2 domains, illustrated in the van der Waals representation (PDB: 7TZC)[35]. Ca^{2+} ions coordinated by calmodulin-1 are also shown. d) Domains of the activation core and channel regions with bound cofactors. The right panel highlights the Ca^{2+}-binding site, showing residues from the CSol and CTD domains and the C3892 mutation site. e) Comparison of closed (PDB: 5TB3) and open (PDB: 5TA3) RyR1 structures, illustrating conformational movements during pore opening[36].

Single-particle cryo-electron microscopy (cryo-EM) studies have resolved near-atomic structures of RyR1 in both the open and closed states[36–41]. RyR1 is a homotetramer, with each protomer comprising three regions: the cytosolic shell, activation core, and transmembrane (TM)

channel; and three regions further divided into 19 domains (Fig. 1a, b)[36,39,41–44]. Recently, the structures of RyR2 and RyR3 have been determined, which reveal a conserved framework[45–47]. Dilation of the pore requires three activators, or co-factors, Ca^{2+}, ATP and caffeine[36]. In the open state, Ca^{2+} binds at the CTD-CSol interface, caffeine at the CTD-S2S3 interface, and ATP (or adenine analogues) at the CTD-S6c-TaF junction (Fig. 1c)[36,48]. Opening involves bending of S6 helices at the glycine hinge (G4934), a rotation that displaces the hydrophobic gate residue (I4937) away from the lumen, and large-scale domain rearrangements (Fig. 1d). Additional regulators include calmodulin-1, which binds via four Ca^{2+} ions, and calstabin-1, both located in the cytosolic shell. The Rycal ARM210 binds cooperatively with ATP in the peripheral RY1&2 (Repeat12) domain of RyR1[35], with a similar mode in RyR2[45,46]. These findings clarify how ARM210 engages RyRs but raise the key question of how drug binding at the most distal RY1&2 domain transmits long-range allosteric stabilization of the pore in the closed state. Elucidating this mechanism will be critical for optimizing next-generation RyR-targeted therapeutics.

This study aims to elucidate how ARM210 allosterically modulates the function of the RyR1 channel at the atomistic level using all-atom explicit solvent molecular dynamics (MD) simulations. Previous MD studies have explored the dynamics of the RyR channel in both its full native and truncated forms, examining gating (opening) mechanism[49–51], ion permeation[52–55], mutations effect on pore gating[56], and interactions with calmodulin and DHPR channels[10,57]. Here, we advance the field by conducting an all-atom MD simulation of the full RyR1 channel over an extensive timescale of 36.6 μs, which required 25 million CPU hours. First, we simulated the wild-type RyR1 channel in the presence of three cofactors, ATP, caffeine, and Ca^{2+} bound within the activation core, and two regulatory proteins, calmodulin-1 and calstabin-1. This revealed long-range allosteric communication spanning over 200 Å along the RyR1 channel, beginning from the peripheral RY1&2 drug-binding domain in the cytosolic shell to the pore-forming S6 helices. To probe the mechanism of ARM210, we simulated the previously described RyR1 complex with drug and ATP bound to RY1&2, uncovering how drug binding reshapes local and global RyR1 dynamics, and in turn, the allosteric network necessary for pore opening. Furthermore, to assess the impact of oxidative stress on RyR1, we studied the cysteine oxidation-mimicking C3892D mutation near the cofactor Ca^{2+} binding site (Fig. 1c), identified through mass spectroscopy, live cell fluorescent microscopy, and single-channel electrophysiology experiments. The simulation of the ARM210-C3892D RyR1 complex showed

that this mutation further perturbs the allosteric network and weakens binding of Ca^{2+} as well as coordination among the associated domains, potentially causing unregulated channel opening.

Results

RyR1 C3892 as a key residue mediating oxidation-induced Ca^{2+} leak. Oxidation of RyR1 increases its open probability under resting conditions, causing sarcoplasmic reticulum (SR) Ca^{2+} leak. RyR1 is highly redox-sensitive, with over 90 cysteine residues per protomer, 21 of which exist as free thiols available for redox modifications[58]. Using mass spectrometry, we identified cysteine residues oxidized upon *in vitro* treatment of purified RyR1 with 50 μM H_2O_2, affecting primarily eight residues (Fig. 2a, Supplementary Table 1). Higher H_2O_2 concentrations caused substantial RyR1 aggregation and were not analyzed (Fig. S1a in Supplementary Information, SI). Notably, four cysteines were near critical regulatory sites: one near the Rycal binding site (C906) and three near the Ca^{2+} binding site (C3733, C3892, C3973), likely impacting activation and channel gating (Fig. 2a). Previously it was shown that residue C906 participates in ARM210 binding[35], and the mutation C906A does not prevent the oxidation-induced leak but partially impairs Rycal protection, consistent with its role in drug binding[35].

To evaluate the functional relevance of the Ca^{2+} site cysteines, we generated single-point alanine mutants (C3733A, C3892A, C3973A) in HEK293 cells, treated them ± H_2O_2, and isolated microsomes. H_2O_2 significantly increased open probability (P_o) in wild-type and all mutants except C3892A, highlighting its central role in oxidation-induced leak (Fig. 2b, Fig. S1b–c in SI). We then analyzed Ca^{2+} leak of wild-type RyR1 and mutant channels and the protective effect of ARM210 by measuring the SR Ca^{2+} store content using live cell fluorescent microscopy. H_2O_2 reduced SR Ca^{2+} stores of cells expressing wild-type but not in RyR1-C3892A mutant channel, and ARM210 prevented depletion in wild-type (Fig. 2c). Mutation of C3892 to aspartic acid (C3892D) mimicking oxidation increased basal P_o and depleted SR Ca^{2+} stores, indicating a gain-of-function modification and that this residue is crucial in the redox regulation of channel gating (Fig. 2b–c, Fig. S1b–c in SI). Therefore, we hypothesize that oxidation to sulfenic, sulfinic, or sulfonic acid or aspartate substitution at C3892 alters electrostatics near the Ca^{2+} binding site, affecting Ca^{2+} coordination and inducing conformational changes that affect pore opening. These findings suggest that the Ca^{2+} binding domain may serve as a redox sensor for oxidative stress, with many functional oxidative residues positioned nearby to enable rapid modulation of

RyR1 activity by adjusting its affinity for binding and coordinating Ca^{2+} ions. We tested this hypothesis using all-atom molecular dynamics simulations.

a

Cysteine #	Nearby domain	Peptide sequence detected by MS
C305	N/A	TEDQGLVVVDA**C**KAHTK
C906	ATP-Rycal	LHP**C**LVNFHSLPEPER
C1781	Calstabin	HHFSPP**C**FVAALPAAG
C3193	N/A	LRPALGE**C**LAR
C3278	Protomer interface	HVIEITLPML**C**SYLPRWWER
C3733	Calcium	S**C**HLEEGGENGEAEEEE
C3892	Calcium	FLQLL**C**EGHNNDFQNYLR
C3973	Calcium	QVFNSLTEYIQGP**C**TGNQR

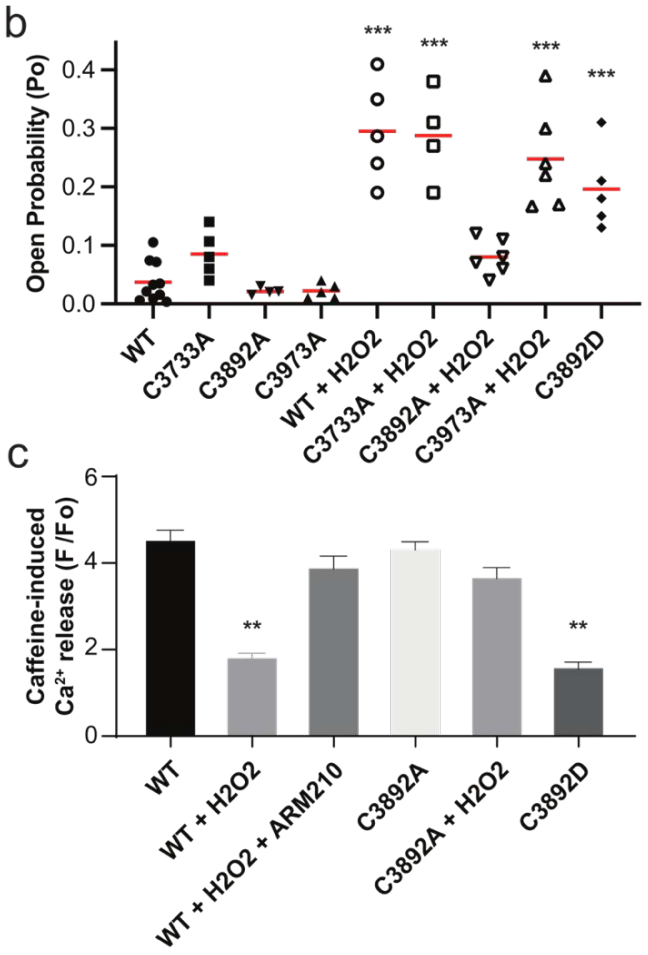


Figure 2: Identification of C3892 as the key residue mediating oxidation-induced Ca^{2+} leak. a) Table listing the main cysteine residues oxidized in purified RyR1 following H_2O_2 treatment, as determined by mass spectrometry. b) Open probability (P_o) of wild-type (WT) RyR1 and cysteine mutants (C3733A, C3892A, C3973A, C3892D) in the absence and presence of H_2O_2. ***$p < 0.001$ c) Sarcoplasmic reticulum Ca^{2+} content measured by caffeine-induced Ca^{2+} release (F/F_0) in HEK293 cells expressing WT RyR1, C3892A, or C3892D in the absence and presence of H_2O_2 or following Rycal ARM210 treatment. **$p < 0.01$ compared to WT RyR1 ($n > 30$).

Extensive molecular dynamics simulations of full-length RyR1. Previous RyR1 molecular dynamics simulation studies often relied on truncated transmembrane models, and even full-length simulations rarely exceeded a few hundred nanoseconds[10,49–55,57]. In this work, full-length RyR1 simulations were performed under three conditions: i) with three activators, ATP, Ca^{2+}, and caffeine bound to the activation core, representing optimal pore opening conditions; ii) with ARM210 and ATP cooperatively bound to the peripheral RY1&2 domain, stabilizing the closed channel; and iii) identical to (ii) but with the C3892D mutation in the CSol domain at the Ca^{2+} binding site, which potentially disrupts ARM210 action and promotes SR Ca^{2+} leak. For each system, three independent trajectories totaling 12.2 μs were generated.

ARM210 remains bound to the RY1&2 domain but adopts multiple binding states. To assess binding stability, we measured ligand occupancy within the binding cavity, representing the fraction of time each molecule remained bound (Fig. 3a). ARM210 largely remained bound in the RY1&2 domain, with only occasional dissociation events in both wild-type and mutant RyR1. ARM210 quickly departed from its initial cryo-EM binding pose and sampled alternative poses within the binding pocket, showing minimal coordination with the residues seen in the structural model (Fig. S2a in SI). Notably, the resolution of the drug-binding domain was lower (3.1 Å) than the overall structural (2.45 Å) in the reported structure[35], suggesting that the reported pose may not be perfectly accurate. While W882 was confirmed as a critical contact residue for ARM210 binding[35], density ambiguity prevents clear assignment of other interacting residues. Our analyses revealed that several additional hydrophobic residues engage ARM210 with comparable frequency (Fig. S3a in SI). Moreover, upon ATP release, ARM210 also contacted ATP-binding residues W996 and H993.

Similarly, ATP molecules cooperatively bound with ARM210 in the RY1&2 domain rapidly drifted from their initial poses, adopting alternative poses with reduced coordination to the original residues before exiting the pocket (Fig. 3a, and Fig. S2a in SI). In addition to the confirmed W996 contact[35], several basic residues R886, R897, R1000, and R1020 were also implicated in ATP binding (Fig. S3b in SI). The three cofactors (ATP, caffeine, and Ca^{2+}) in the activation core displayed distinct stabilities: ATP remained bound throughout all simulations, Ca^{2+} was generally stable but occasionally dissociated, and caffeine exhibited the weakest binding, often dissociating from the pocket (Fig. 3a, Fig. S2b in SI). Detailed analyses of these interactions are provided in section S2 of SI.

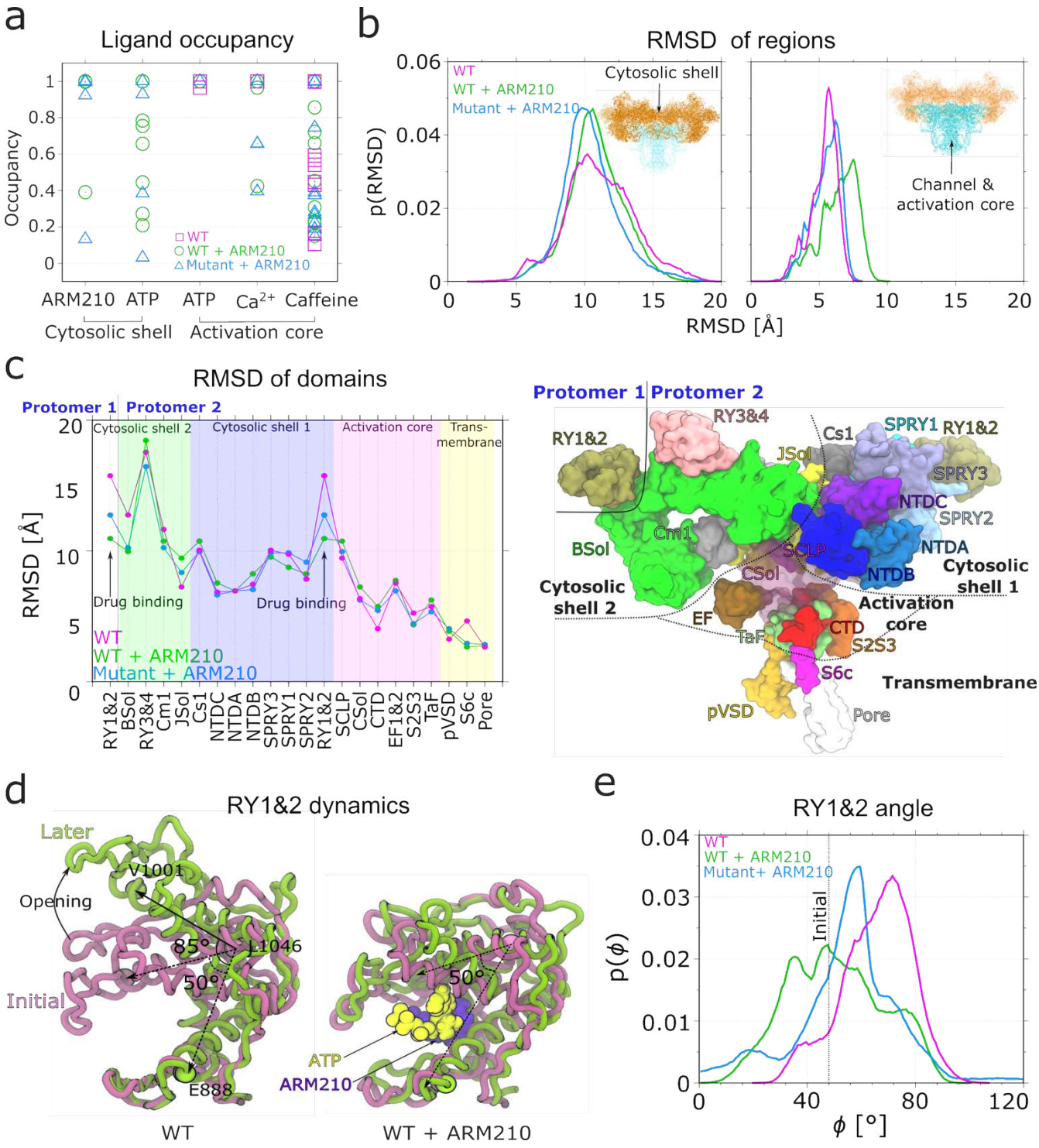


Figure 3: Ligands binding and domain dynamics of the RyR1 channel. a) Occupancy of ARM210 and cofactors within their binding pockets, where 1 indicates continuous binding and 0 indicates absence. b) Probability distribution of backbone RMSD for cytosolic shell region (left) and the activation core plus channel regions (right) across the three simulated systems. c) Average backbone RMSD of all RyR1 domains and regulatory proteins (calmodulin-1, Cm1; calstabin-1,

Cs1) in the three systems. Domains and proteins are grouped by spatial location in four regions: cytosolic shell 2, cytosolic shell 1, activation core and transmembrane channel, highlighted by background shading, and also shown over the RyR1 protomer on right panel. RY1&2 domain is shown multiple times on both panels, with repeated RMSD values on the plot. d) Left: opening of the RY1&2 domain in the absence of ARM210 and ATP, comparing the initial closed state (pink) to the later opened state (green) in the simulation. The angle between residues E888, L1046 and V1001 increases from 50 to 85°. Right: RY1&2 domain remains closed when ARM210 and ATP are bound. e) Probability distribution of the RY1&2 domain angle (ϕ), as defined in the panel d, for the three simulated systems.

ARM210 binding rigidifies the cytosolic shell of RyR1. Across the three systems, the cytosolic shell showed larger fluctuations, with root mean square deviation (RMSD) values reaching ~18 Å, compared to ~9 Å for the activation core plus transmembrane regions (Fig. 3b). Notably, cytosolic shell deviations were reduced in the presence of ARM210, with similar RMSD values for both wild-type and mutant channels. In contrast, the absence of the drug led to pronounced oscillations, suggesting that ARM210 binding stabilizes the cytosolic shell. The activation core and transmembrane channel regions displayed greater deviation in the presence of the drug, particularly in the wild-type channel, but the underlying cause remains unclear.

Next, we assessed the RMSD of RyR1 domains along with the regulatory proteins calmodulin-1 and calstabin-1 (Fig. 3c). For this analysis, RyR1 was divided into four regions: cytosolic shell 1, cytosolic shell 2, activation core, and transmembrane, according to the spatial arrangement of associated domains and proteins, where the drug-binding RY1&2 domain from a neighboring protomer is also included. The RY1&2 domain interacts with cytosolic shell 2 region of the adjacent protomer, and in the absence of ARM210, these regions exhibited large fluctuations, explaining elevated cytosolic shell RMSD in Fig. 3b. Most importantly, the RY1&2 domain showed the highest fluctuation among all components, highlighting its potential role in regulating RyR1 dynamics. In contrast, the cytosolic shell 1 (excluding RY1&2), activation core, and transmembrane regions displayed no consistent RMSD trends. A few domains within the activation core (SCLP, CSol, CTD, and TaF) oscillated slightly more in the drug-bound wild-type system, contributing to the modest RMSD increase in the activation core and transmembrane regions (Fig. 3b), but these fluctuations were far less pronounced than those in the cytosolic shell.

ARM210 restricts opening of the RY1&2 domain. The RY1&2 domain exhibits significantly higher mobility than other regions of RyR1 (Fig. 3c). In the absence of ARM210, it undergoes substantial conformational changes, opening in a "jaw-like" manner, whereas binding of ARM210 and ATP stabilizes the domain in a closed state (Fig. 3c, Movie S1). To quantify this behavior, we measured the angle ϕ defined by residues E888, L1046, and V1001. Starting from ~50° in the cryo-EM state, the RY1&2 domain shifted towards ~85° without the drug. In contrast, with ARM210, this domain predominantly remained near 50° in both wild-type and mutant RyR1, occasionally closing further towards 0°, a behavior never observed in the drug-free state.

ARM210 binding and C3892D mutation modulate RyR1 domain dynamics. Upon activation by the cofactors, RyR1 undergoes extensive global conformational changes. Two primary motions occur during the closed-to-open transition: (i) translational shifts, where regions or domains move up or down along the pore axis, and (ii) rotational motions, where regions or domains rotate clockwise or anticlockwise relative to the membrane plane (a plane orthogonal to the pore axis), as viewed from the cytosolic side. Comparison of closed and open cryo-EM structures indicates that cytosolic shell regions 1 and 2 move downward toward the pore, while the activation core and transmembrane region shift upward (Fig. S4a–b in SI). Additionally, the cytosolic shell and activation core rotate anticlockwise, whereas the transmembrane region exhibits a slight clockwise rotation (Fig. S4c–d in SI). In our simulations, most regions and domains display both translational and rotational movements in both directions; because full dilation of the pore was not achieved in any system, we will focus on average domain movements for comparative analyses among the three systems.

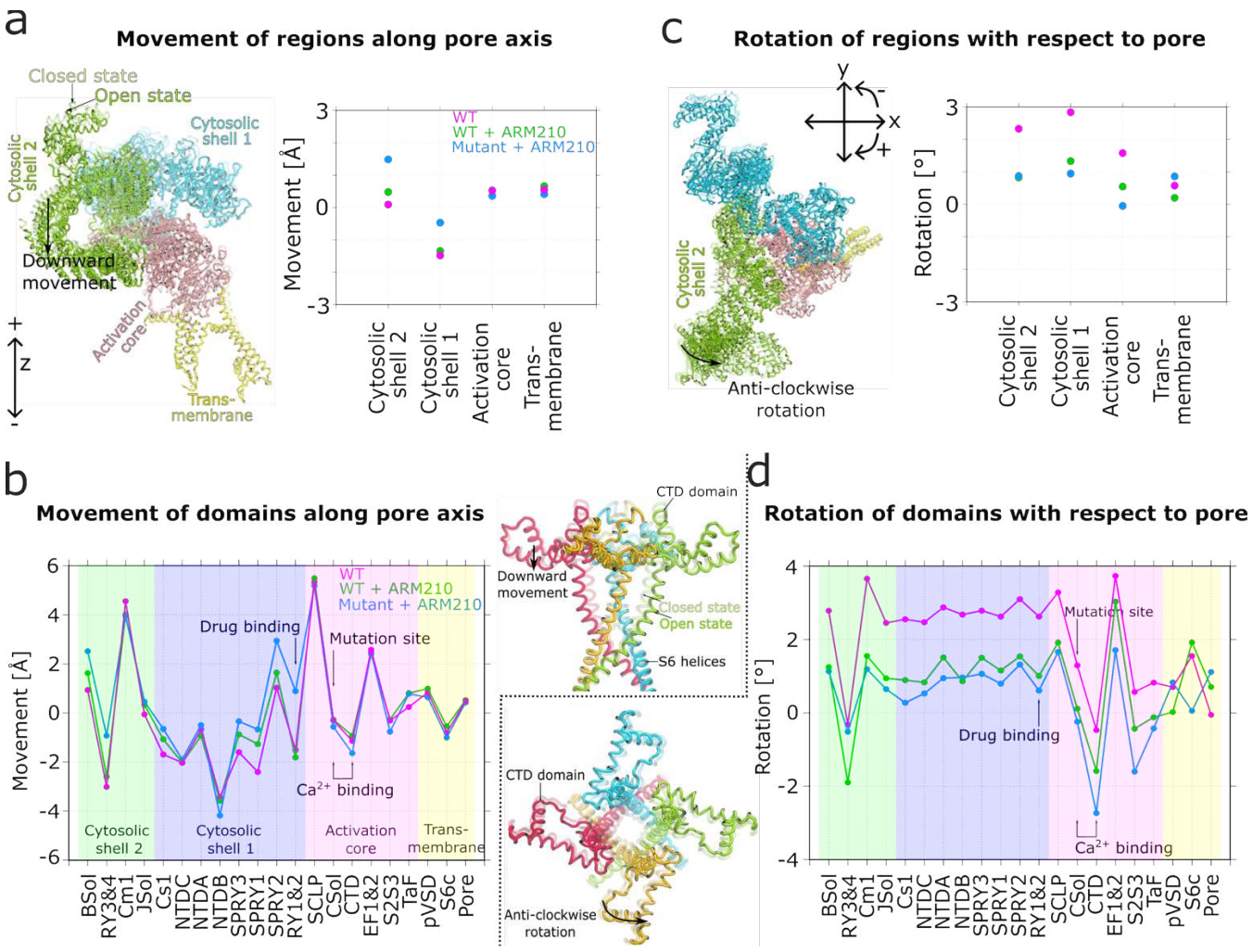


Figure 4: Translational and rotational dynamics of RyR1 during MD simulations. a) Left: Translational displacement of the cytosolic shell 2 region along the pore axis (z-axis) between closed to open cryo-EM states (PDBs: 5TB3, 5TA3), showing downward (-z) shift. Right: Average translational movements of the four structural regions (cytosolic shell 1, cytosolic shell 2, activation core, and transmembrane) relative to the initial 0 Å position across three simulated systems. b) Left: Average translational movements of all domains and regulatory proteins (calmodulin-1 and calstabin-1) relative to the initial 0 Å position across three systems. Right: Translational displacement of the CTD domain along the pore axis during closed-to-open transition in cryo-EM states, showing a downward shift. c) Left: Anticlockwise rotation of the cytosolic shell 2 region during pore opening in cryo-EM states (negative rotation in xy-plane). Right: Average rotational motions of the four RyR1 regions relative to the initial 0° across three simulated systems. d) Left: Anticlockwise rotation of the CTD domain during the closed-to-open transition in cryo-EM structures. Right: Average rotational motions of all RyR1 domains and regulatory proteins, referenced to initial 0° orientation, compared across three simulated systems.

In wild-type RyR1 without ARM210, the cytosolic shell regions 1 and 2 along with several associated domains (BSol, JSol, RY3&4, NTDC, SPRY1/2/3/) and the regulatory protein

(calstabin-1) had a more pronounced downward shift compared to both wild-type and mutant channels in the presence of ARM210, in agreement with the channel being in the primed state due to the presence of activating cofactors (Fig. 4a & c). ARM210 binding induced a modest upward shift in the wild-type protein, whereas the mutant exhibited a substantially larger upward displacement for these cytosolic domains. This upward shift is in agreement with the conformational changes observed by cryo-EM for RyR2 variants in the presence of ARM210[45,46]. The activation core and the transmembrane regions, taken as whole, displayed a net upward movement in all three systems (Fig. 4a). At the domain level, however, approximately half of the domains moved upward while the others shifted downward (Fig. 4c). Whereas wild-type RyR1 showed no major differences between the drug-free and drug-bound states, the mutant in drug-bound form revealed a distinct behavior: the Ca^{2+}-binding CSol and CTD domains, both critical regulatory sites, with CSol also harboring the mutation, along with the S2S3 domain exhibited greater downward shifts. Similarly, within the transmembrane region, the S6c helices shifted downward more prominently in the mutant compared to wild-type systems. These findings are consistent with the fact that the Rycal drug preferentially affects the leaky (mutant and/or PMT modified) channels compared to the wild type non-leaky channels. This contributes to the lack of off target activities of the Rycal drugs.

Compared to the translational shifts, notable differences were observed in rotational dynamics across the systems. In wild-type RyR1, cytosolic shell regions 1 and 2 displayed substantial clockwise rotations of 2.8° and 2.3°, respectively, which were reduced to 1.3° and 0.8° upon ARM210 binding (Fig. 4d). In the mutant, ARM210 further limited rotation of cytosolic shell 2 (0.9°), while cytosolic shell 1 remained similar to the drug-bound wild-type (0.8°). At the domain level, nearly all cytosolic domains, except RY3&4, showed pronounced clockwise rotation in the absence of drug, which were consistently suppressed upon ARM210 binding in both protein variants (Fig. 4f). The previously described “jaw-like” opening of the RY1&2 domain in the absence of ARM210 can be interpreted as a clockwise rotation of half the domain (Fig. 3d). This movement subsequently propagated clockwise rotational motion throughout the cytosolic shell. Importantly, RY1&2 opening in one protomer induces rotation in the cytosolic shell of the neighboring protomer. Conversely, ARM210 binding prevents RY1&2 opening and thereby rigidifies the entire cytosolic shell. These findings highlight RY1&2 as a critical regulator that

synchronizes rotational dynamics across protomers, especially in cytosolic shell regions (see Movie S1).

Variations in rotational dynamics were also evident in the activation core. In wild-type RyR1, the activation core rotated approximately 1.6° clockwise, which was reduced to 0.5° upon ARM210 binding, while in the drug-bound mutant it rotated slightly in the anticlockwise direction (-0.1°), see Fig. 4d. At the domain level, most activation core domains rotated clockwise, except the CTD, which rotated anticlockwise (-0.5°) in wild-type RyR1 (Fig. 4f). Similar to its effects on the cytosolic regions, ARM210 binding in both protein variants restricted rotation of several activation core domains (SCLP, CSol, EF1&2), while others (CTD, S2S3, TaF) reversed direction entirely. Among these, the CTD domain, closely interacting with the mutation-bearing CSol domain, was particularly notable, showing enhanced anticlockwise rotation (-1.6°) in the drug-bound wild-type protein and an even larger shift in the mutant (-2.7°). Likewise, S2S3 and TaF domains also exhibited similar exaggerated anticlockwise motion in the mutant, suggesting that the C3892D mutation induces aberrant behavior in activation core dynamics. In contrast, movements in the channel region domains were more limited and largely random across all systems.

RY1&2 domain allosterically regulates RyR1 pore opening. Allosteric communication in proteins involves networks of coupled dynamics, where perturbations, such as drug binding or mutations at one site, propagate conformational changes to distant regions through correlated motions, thereby enabling signal transmission. To investigate correlated motions in the wild-type RyR1 without drug, we constructed a correlation matrix based on the center-of-mass displacements of all domains and regulatory proteins (calmodulin-1 and calstabin-1) in the xy-plane. Each matrix element represents the Pearson correlation coefficient between domain pairs (Fig. 5a-b). As noted earlier, domain rotations in the xy-plane depend on the opening of the adjacent protomer's RY1&2 domain. Accordingly, the RY1&2 domain from a neighboring protomer was included in the analysis, and correlations were computed exclusively from xy-plane motions to capture this inter-protomer coupling.

We see strong intra-regional correlations across all four regions of wild-type RyR1. Domains within the cytosolic shell 2 region display particularly strong correlations, followed by cytosolic shell 1 and the activation core, with weaker correlations in the transmembrane region. In

contrast, inter-regional correlations are more selective: the cytosolic shell 2, activation core, and transmembrane regions (excluding the pore domain) are strongly coupled, whereas the cytosolic shell 1 region shows minimal connectivity with other regions. Inclusion of the neighboring protomer's RY1&2 domain reveals that it further reinforced the correlated network linking cytosolic shell 2, the activation core, and the transmembrane region (Fig. 5c). These results indicate that motions originating in the RY1&2 domain of one protomer allosterically propagate through cytosolic shell 2, into the activation core, and ultimately reach the pore-forming S6c helices of the adjacent protomer. We propose that this long-range allosteric pathway (Fig. 5d), extending over a distance greater than 200 Å, is essential for driving pore dilation.

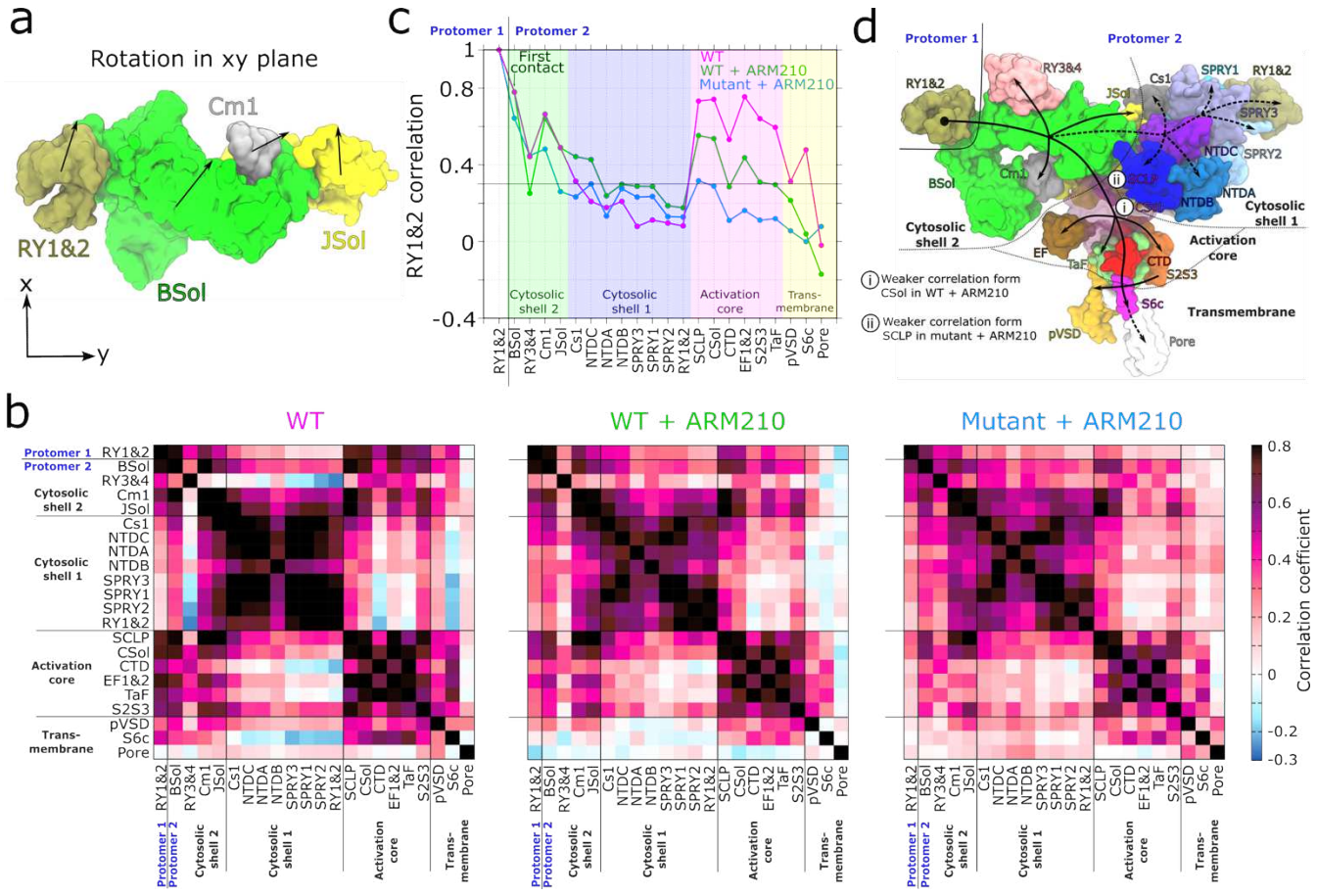


Figure 5: Correlated motions of RyR1 domains and regulatory proteins. a) Selected RyR1 domains are shown with displacement vectors representing center-of-mass shifts in the xy-plane relative to their initial positions. These vectors were used to compute correlation coefficients between domain pairs. b) Pearson correlation coefficient matrices depicting inter-domain correlations within RyR1 and the bound regulatory proteins calmodulin-1 and calstabin-1 across the three systems. The drug-binding RY1&2 domain from the adjacent protomer (protomer 1) is also included. c) Correlation coefficients between RY1&2 domain of protomer 1 and all other

domains/proteins of protomer 2, extracted from the first row of matrices in panel b, compared across the three systems. d) Network representation of correlations from panel c for wild-type RyR1 without drug. Solid lines indicate strong correlations (> 0.3), and dotted lines indicate weaker correlations. Positions i and ii highlight domains from where weaker correlations were observed in the drug-bound wild-type and mutant proteins, respectively.

ARM210 disrupts the allosteric network required for pore opening. In the ARM210-bound wild-type RyR1, the overall correlation matrix closely resembles that of the drug-free state, but with the slightly reduced intra-regional correlations across all four regions (Fig. 5b, Fig. S7 in SI). Inter-regional correlations are more strongly affected, showing a marked decline relative to the unbound system. Notably, the correlation between the neighboring protomer's RY1&2 domain and the cytosolic shell 2 region of the current protomer remains robust, similar to the drug-free state; however, the correlation weakens substantially beyond the activation core (Fig. 5c, Fig. S7 in SI). In particular, beyond the CSol domain within the activation core, correlations diminished sharply, suggesting that allosteric propagation is disrupted from this junction. These findings indicate that ARM210 binding prevents the RY1&2 domain from effectively transmitting its motion through the downstream allosteric network, particularly from the CSol, thereby blocking the cascade of conformational changes that would otherwise reach the S6c helices (Fig. 5d). Consequently, ARM210 stabilizes the pore in a closed conformation, a result supporting its role as an allosteric modulator of RyR1 that prevents a pathological leak of Ca^{2+} in the mutant and PTM modified channels.

The C3892D mutation disrupts the allosteric network and displaces Ca^{2+} and the CTD domain. The correlation matrix of the ARM210-bound C3892D RyR1 mutant resembles that of the drug-bound wild-type protein, but with the further weakened intra- and inter-regional correlations (Fig. 5b, Fig. S7 in SI). While the RY1&2 domain maintains a strong correlation with the cytosolic shell 2 domains of the neighboring protomer, this correlation rapidly collapses beyond the first activation core domain, SCLP (Fig. 5c–d). This indicates that the C3892D mutation in the CSol domain exacerbates the disruption of the allosteric signaling pathway already impaired by the ARM210 binding. In theory, such an amplified breakdown of communication should further stabilize the closed state and suppress pore opening. Paradoxically, experimental observations reveal that the mutant pore occasionally becomes leaky, with an opening probability of 0.2 compared to 0.04 in the wild type (Fig. S1c in SI). This

suggests that the mutation not only destabilizes the allosteric network but may also cause perturbations in the structural positioning of key elements.

This prompted us to further investigate how the C3892D mutation alters Ca^{2+} affinity and the coordination of the associated CSol and CTD domains. In the wild-type RyR1, Ca^{2+} occupancy near residue C3892 is negligible, but in the mutant it rises to approximately 0.35 (Fig. 6a). This shift reduces Ca^{2+} interactions with its native coordinating residues, E3893, E3967, T5001, and E5002, within the CSol and CTD domains. As a result, Ca^{2+} is displaced, weakening the interactions at CSol-CTD interface, and driving the CTD domain away from the CSol domain (Fig. 6b–c). Consistent with this finding, the CTD domain in the mutant shows a pronounced downward displacement toward the pore and exaggerates anticlockwise rotation compared to both drug-free and drug-bound wild-type proteins (Fig. 4c–f). Together, these findings indicate that the CTD domain becomes misaligned, escaping regulatory influence of the surrounding cytosolic shell and activation core. This miscoordination propagates directly to the adjacent S6 helices, key elements in pore dilation, thereby compromising gating dynamics.

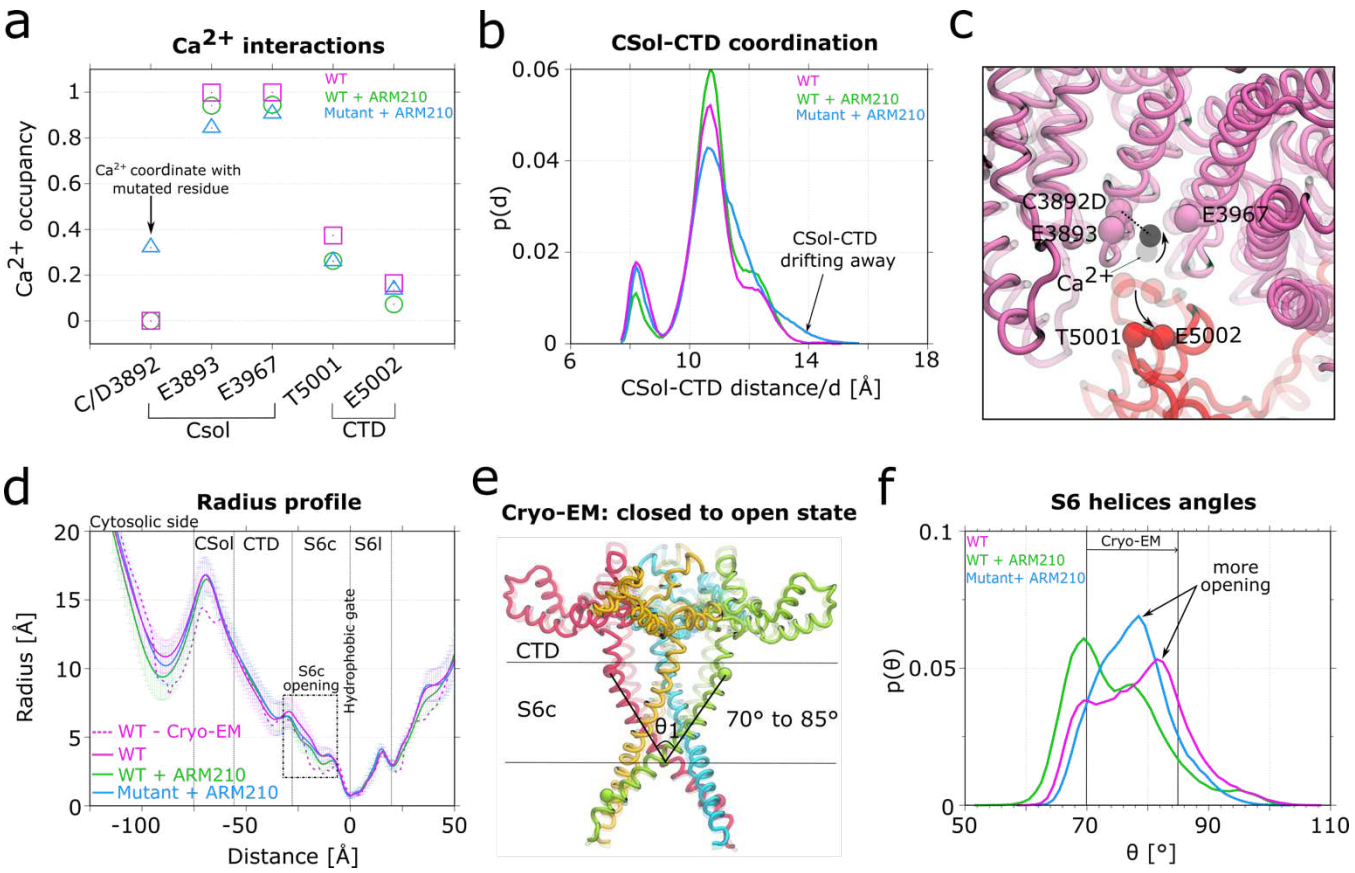


Figure 6: Effects of the C3892D mutation on Ca^{2+} binding, coordination of domains, and pore opening. a) Ca^{2+} occupancy near the binding-pocket residues of the CSol and CTD domains across three simulated systems. b) Probability distributions of the CSol–CTD interdomain distance for the three systems. c) Representative snapshot showing displacement of Ca^{2+} toward the mutated C3892D residue in the CSol domain, leading to weakened Ca^{2+} coordination and displacement of the CTD domain. The translucent structure represents the initial configuration; the opaque structure depicts the later structure. d) Average pore-radius profiles along the RyR1 pore axis for all three systems, compared with the cryo-EM closed-state structure (PDB: 5TB3)[36]. e) Cryo-EM structures illustrating S6 helix opening during the closed-to-open transition, highlighting expansion at the cytoplasmic side (S6c), quantified as angle θ_1 (translucent = closed state, opaque = open state). f) Probability distributions of θ_1 for the three systems, with vertical lines marking the closed and open cryo-EM reference states.

S6c helices open more extensively in the C3892D mutant bound to ARM210. Pore dilation in RyR1 is mediated by bending and distortion of the four S6 helices, particularly from the central hinge at G4934 to the cytosolic-facing region known as the S6c domain. Average pore-radius profiles across all three systems reveal a notable increase in the radius at the S6c region (Fig. 6d). Among these, the wild-type channel without ARM210 displays slightly greater dilation than both drug-bound systems. Between the two drug-bound systems, however, the mutant exhibits noticeably larger dilation than the wild type, explaining the gain-of-function properties observed.

To quantify this effect, we measure the angle (θ_1) between the opposing S6c helices, which increases from ~70° in the closed state to ~85° in the fully open state according to cryo-EM structures (Fig. 6e). Across simulations, the largest angular changes were observed in the wild-type protein without drug (Fig. 6f, Fig. S5 in SI). Notably, in the presence of ARM210, the mutant channel exhibits a modest but consistent increase in θ_1 compared to the drug-bound wild type, suggesting that the pore is pushed toward dilation more readily in the mutant.

These observations reinforce the earlier conclusion that dysregulation of the CTD domain destabilizes the closed state by accelerating opening of the S6c helices in the mutant. This is consistent with experimental findings showing that the mutant has a higher open probability (0.2 vs. 0.04 in the wild type; Fig. S1c in SI). Finally, it is worth noting that while the S6c helices undergo significant bending and partial opening, the luminal-facing S6l helices, as expected, exhibit only minimal angular changes, and dilation at the hydrophobic gate is not achieved in all simulations (Fig. S6 in SI).

Discussion

New insights into the role of cofactors and drug in RyR1 dynamics. Engagement of all three activators (Ca^{2+}, ATP, and caffeine) at the CTD interfaces initiates a structural reorganization of the RyR1 activation core domain, referred to as "priming", that facilitates subsequent pore dilation[36,59]. Across all simulations, ATP and Ca^{2+} consistently displayed strong binding affinities and coordination patterns closely resembling those observed in cryo-EM structures. In contrast, caffeine exhibited relatively weak affinity, frequently dissociating from its binding pocket (Fig. 3a, Fig. S2 in SI). These computational findings align with the experimental data showing that the RyR1 open probability is <0.25 under conditions of Ca^{2+} alone or ATP with caffeine, but increases to >0.9 when all three activators are present [36,59,60]. This underscores the critical requirement for both high-affinity cofactors, ATP and Ca^{2+}, to drive the conformational rearrangements that couple interacting domains and stabilize the primed state. Caffeine, while a weaker ligand, further reinforces this primed conformation, effectively lowering the energetic barrier to pore dilation and sustaining channel opening.

Each peripheral drug binding RY1&2 domain of RyR1 can accommodate either one ARM210 molecule together with one ATP, or alternatively two ADP molecules[35]. In our simulations, ARM210 predominantly remained bound within the RY1&2 pocket; though it diffused locally and

adopted multiple poses distinct from the one displayed in the cryo-EM map (Fig. 3a, Fig. S2 in SI). ATP displayed similar mobility within the pocket but was more prone to slipping out of the binding site. Given the previously reported low resolution of this region[35], it is likely that the cryo-EM–annotated binding poses are not fully accurate. Considering that ARM210 and ATP share structural similarity, and that two ADP molecules can occupy the pocket with one positioned where ARM210 binds, it is plausible that ARM210 and ATP may occasionally exchange binding positions.

ARM210 predominantly occupied the RY1&2 domain during simulations, inducing pronounced changes in its dynamics and, consequently, in the entire cytosolic shell. In the absence of ARM210 and the associated ATP, the RY1&2 domain opened rapidly (within ~100 ns) in a jaw-like motion (Fig. 3). While the half of the domain adjacent to the ATP-binding site remained relatively stable, the other half, which accommodates ARM210, underwent substantial displacement. This opening slightly exceeded that reported in previous structures by ~10°–15° and persisted for the majority of the simulation[40,42–44]. In contrast, the presence of ARM210 and ATP maintained the RY1&2 domain in a closed state, consistent with the cryo-EM structures[35,45]. Notably, the domain occasionally closed even further following ATP release.

The cytosolic extensions of the S6 helices (S6c) undergo bending, bowing, and distortion originating from the gating hinge (G4934), accompanied by a rotation that reorients the sidechains of the hydrophobic gate residue, I4937, away from the lumen to permit Ca^{2+} passage during transition to the open state[36,39,61]. Similar bending and bowing of the S6c helices were observed across all simulations. The wild-type RyR1 channel frequently adopts this open-like conformation of S6c helices in the absence of ARM210, indicating that the channel reaches the dilated state more readily without the drug (Fig. 6). In the C3892D mutant, S6c helices achieved an open-like state even in the presence of ARM210, suggesting that the mutation perturbs channel dynamics. Notably, no movement or opening of the hydrophobic gate residue I4937 was observed, as the bending and bowing of S6c did not propagate to the hinge residue G4934; significant motion was limited to the distal S6c region (G4941–T4956). These findings indicate that distal S6c rearrangements can occur with or without drug binding, but full pore opening requires propagation of motion to the central S6 region, including the hydrophobic gate and the hinge, which represent the rate-limiting steps.

Mechanism of allosteric regulation in RyR1. Although full pore dilation was not achieved in any of our simulations, the conformational changes in the peripheral regions of RyR1 provided significant insights into correlated motions and the allosteric pathways. Differences in the flexibility and opening of the RY1&2 domain in response to drug binding were found to modulate the dynamics of the entire cytosolic shell. In the absence of ARM210, the opening of the RY1&2 domain, manifested as the displacement of the ARM210-interacting region, can be visualized as a clockwise rotation from the cytosolic viewpoint (Fig. 4). This rotation initiates a domino effect across the cytosolic shell of the adjacent protomer, inducing a coordinated clockwise rotation of all domains and associated proteins, including calmodulin-1 and calstabin-1, and resulting in highly correlated movements. Such synchronized motion mirrors the closed-to-open state transition observed in cryo-EM structures[36,39]. The RY1&2 motion exhibits strong correlation with half of the cytosolic shell in the neighboring protomer, designated as cytosolic shell 2, which comprises BSol, RY3&4, JSol domains, and calmodulin-1. These correlated motions further extended, though more weakly, to the activation core domains (SCLP, CSol, EF, TaF, S2S3, CTD) and the transmembrane S6c domain, while correlation with cytosolic shell 1 (NTD-A/B/C, SPRY1-3, RY1&2) remained minimal (Fig. 5, Fig. S7 in SI). Similar patterns were observed in three-dimensional correlated motions, including translation along the z-axis and rotation in the xy-plane (Fig. S8 in SI).

Based on these observations, we propose an allosteric pathway that facilitates pore dilation in wild-type RyR1 (Fig. 7, left panel). Initially, the tetrad of $Ca_v1.1$ voltage-gated Ca^{2+} channels activates RyR1 via interacting with the RY3&4 domains[10]. This activation signal, amplified by the dynamic behavior of the RY1&2 domain from the neighboring protomer, is transmitted downstream to the transmembrane pore region. Extensive opening of the unoccupied RY1&2 domain triggers correlated rearrangements through the cytosolic shell 2 region, then to the activation core, and ultimately to the pore-forming S6c helices in the adjacent protomer. In the presence of the three activators (ATP, Ca^{2+}, and caffeine) bound to the activation core, these allosteric signals facilitate pore dilation, allowing Ca^{2+} release from the sarcoplasmic reticulum into the cytoplasm. This long-range allosteric pathway, spanning approximately 200 Å from the RY1&2 to S6c across protomers, underpins the functional regulation of RyR1 channel gating.

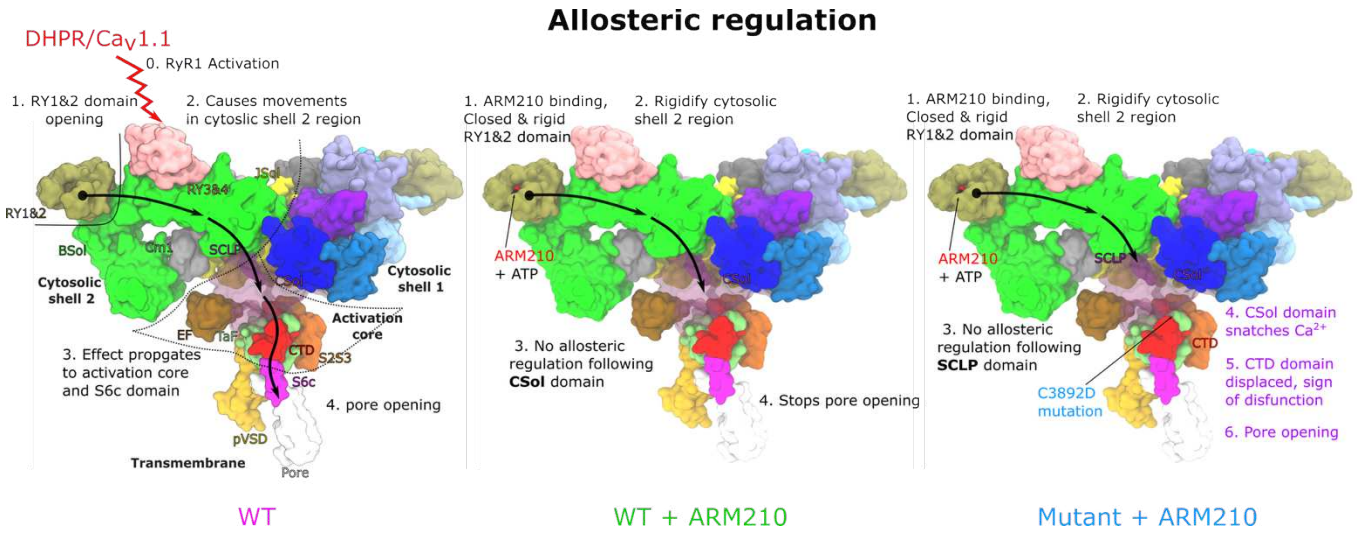


Figure 7: Schematic representation of the allosteric network and the sequence of events in wild-type RyR1, ARM210-bound RyR1, and ARM210-bound C3892D mutant RyR1. The diagrams highlight how dynamic changes in the drug-binding RY1&2 domain propagate through the RyR1 protein, triggering a cascade of conformational rearrangements that ultimately modulate the opening or closing of the channel pore.

Allosteric modulation of RyR1 dynamics by ARM210. The cooperative binding of ARM210 and ATP within the RY1&2 domain induced profound local and global changes in RyR1 dynamics. This interaction rigidified the RY1&2 domain, stabilizing it in a closed conformation and, in turn, reinforcing the rigidity of the entire cytosolic shell[35,46]. Translational and rotational motions of the activation core and channel regions were also markedly altered compared to the drug-free state. These effects are particularly evident in the correlated motions analysis, where RY1&2 movements strongly correlate with the cytosolic shell 2 region but showed weak correlation with the activation core and channel regions of the adjacent protomer (Fig. 5, Fig. S7 in SI). Notably, beyond the CSol domain of the activation core, correlations weaken substantially, indicating a dampening of downstream signal transmission following ARM210 binding. From these observations, we propose the mechanism of ARM210-mediated allosteric regulation of RyR1 (Fig. 7, middle panel). Upon activation by $Ca_v1.1$ channels through the RY3&4 domains, the ARM210-occupied RY1&2 domain obstructs the transmission of conformational signals to the transmembrane region. The inability of RY1&2 to open locks the cytosolic shell into a highly rigid state, suppressing coordinated rearrangements within cytosolic shell 2, the activation core, and the channel region of the neighboring protomer. Consequently, the allosteric signal originating from the RY1&2 and RY3&4 domains is attenuated as it passes through the CSol

517 domain and fails to effectively reach the pore-forming S6c helices. Thus, ARM210 binding
518 stabilizes the closing of the pore, even in the presence of all three activators within the activation
519 core.

520 **Mutation-driven disruption of ARM210-mediated allosteric regulation in RyR1.** Cysteine
521 oxidative modifications have been shown to alter the gating behavior of ryanodine receptors,
522 leading to dysregulated Ca^{2+} release and impaired channel function[25,62–64]. Among the three
523 cysteine residues (C3733, C3892, C3973) located near the Ca^{2+} cofactor binding site, oxidation
524 of C3892 has the greatest impact on channel gating, as shown by the C3892D mutation, which
525 mimics the oxidized state. In simulations, ARM210 binding to the C3892D mutant RyR1
526 produced effects similar to those in the wild type, including reduced RY1&2 domain opening and
527 rigidification of the cytosolic shell in the adjacent protomer (Figs. 3 and 4). However, critical
528 differences emerged: correlated motions between the RY1&2 domain and components of
529 cytosolic shell 2 (e.g., JSol, calmodulin-1) were already weakened, and correlations with the
530 activation core and channel regions were almost completely lost (Fig. 5, Fig. S7 in SI).
531 Importantly, the mutated residue in the CSol domain pulled the bound activator Ca^{2+} more tightly
532 toward itself, disrupting the coupling between CSol and CTD and causing the two domains to
533 drift apart (Fig. 6). This displacement induced excessive rotations and translational shifts in the
534 CTD and surrounding domains (S2S3, TaF), which in turn promoted further opening of the S6c
535 helices.

536 From these observations, we propose a mechanism for how the C3892D mutation alters
537 ARM210-mediated allosteric regulation (Fig. 7, right panel). Upon activation by $Ca_V1.1$, ARM210
538 binding in the RY1&2 domain still restricted downstream allosteric signaling, but the degree of
539 inhibition was far weaker than in the wild-type. The RY1&2 domain remained closed, yet its
540 coupling to cytosolic shell 2, the activation core, and channel regions was severely
541 compromised, with correlations essentially disappearing from the first activation core domain
542 (SCLP) onward. This loss of communication arose from mutation-induced mispositioning of Ca^{2+}
543 and destabilization of the CTD, which propagated unregulated motions into the S6c helices and
544 surrounding channel elements. Consequently, the mutant channel exhibited dysfunctional
545 dynamics, occasionally permitting pore dilation driven only by ATP and caffeine. We hypothesize
546 that while ARM210 retains some allosteric influence, it is significantly less effective at stabilizing
547 the C3892D mutant RyR1 in the closed state.

Next-generation Rycals. This study highlights that targeting the conserved RY1&2 domain, shared across all RyR isoforms, represents a highly promising strategy for treating RyR-mediated diseases. For the development of next-generation RyR-based therapeutics, the key objective should be to stabilize the RY1&2 domain in its tightly closed conformation for longer periods. This would more effectively block downstream allosteric signaling and prevent pathological channel leakiness. In our view, future molecules should be optimized not only for strong interactions with the RY1&2 binding pocket residues but also with ATP or the ATP-binding pocket. Such dual optimization would allow the compound to have higher affinity in the RY1&2 domain, both in the presence and absence of ATP within the pocket.

Material and Methods

RyR1 purification and oxidation

RyR1 was purified from rabbit skeletal muscle following a protocol previously described by Marks lab[35,65]. All steps were performed on ice unless otherwise stated. Rabbit back and thigh muscles were harvested, snap-frozen in liquid nitrogen immediately after euthanasia, shipped on dry ice, and stored at −80°C (BioIVT). 20 g of skeletal muscle tissue was resuspended in 150ml buffer A (10 mM tris-maleate pH 6.8, 1 mM EGTA, 1 mM benzamidine hydrochloride, 0.5 mM AEBSF) and homogenized in a Waring blender for 3 minutes. The suspension was centrifugated at 11,000 x g for 10 min, and the supernatant was filtered through cheesecloth to remove debris. Following centrifugation at 36,000 x g for 30 min, the pelleted membrane fraction was solubilized in 8 mL of buffer B (10 mM HEPES pH 7.4, 0.8 M NaCl, 1% CHAPS, 0.1% phosphatidylcholine, 1 mM EGTA, 2 mM DTT, 0.5 mM AEBSF, 1 mM benzamidine hydrochloride, one protease inhibitor tablet (Pierce)) followed by homogenization using a glass tissue grinder (Kontes). The homogenate was diluted with buffer C (buffer B without NaCl) at a 1:1 ratio following 10 more strokes of homogenization. After centrifugation at 100.000 x g for 30 min to remove CHAPS-insoluble material, the supernatant was filtered (0.22 µm) and then loaded onto a HiTrap Q HP column (1 mL, GE Healthcare) previously equilibrated with buffer D (10 mM HEPES pH 7.4, 400 mM NaCl, 0.2% CHAPS, 1 mM EGTA, 0.5 mM TCEP, 0.01% 1,2-dioleoyl-sn-glycero-3-phosphocholine (DOPC, Avanti), 0.5 mM AEBSF, and 1 mM benzamidine hydrochloride). After washing with six column volumes of buffer D, the immobilized protein on the HiTrap Q HP column was eluted with a linear gradient from 480 to 520 mM NaCl using a linear mix of buffer D and

buffer E (buffer D with 600 mM NaCl). RyR1-containing fractions were incubated for 30 minutes with H_2O_2 at concentrations of 50, 100, 150, and 250 μM before immediately separating them on 4-12% gradient SDS-PAGE and sent for mass spectrometry analysis to in-house Columbia Proteomics Shared Resource (HICCC).

Mass spectrometry

Protein gel slices were excised and subjected to in-gel digestion as previously described[66], with minor modifications. Digested peptides were collected and further extracted from gel slices in extraction buffer (1:2 ratio by volume of 5% formic acid: acetonitrile) at high speed, shaking in an air thermostat. Peptides were separated within 80 min at a flow rate of 400 nl/min on a reversed-phase C18 column with an integrated CaptiveSpray Emitter (25 cm x 75μm, 1.6 μm, IonOpticks). Mobile phases A and B were with 0.1% formic acid in water and 0.1% formic acid in ACN. The fraction of B was linearly increased from 2 to 23% within 70 min, followed by an increase to 35% within 10 min and a further increase to 80% before re-equilibration. The timsTOF Pro was operated in PASEF mode[67] with the following settings: Mass Range 100 to 1700m/z, 1/K0 Start 0.6 V·s/cm2, End 1.6 V·s/cm2, Ramp time 100ms, Lock Duty Cycle to 100%, Capillary Voltage 1600V, Dry Gas 3 l/min, Dry Temp 200°C, PASEF settings: 10 MSMS Frames (1.16 seconds duty cycle), charge range 0-5, active exclusion for 0.4 min, Target intensity 20000, Intensity threshold 2500, CID collision energy 59eV. A polygon filter was applied to the m/z and ion mobility plane to select features most likely representing peptide precursors rather than singly charged background ions. Acquired PASEF raw files were analyzed using the MaxQuant environment v.2.0.1.0 and Andromeda for database searches at default settings with a few modifications[67]. MaxQuant was set up to search with the reference human proteome database downloaded from UniProt. The following modifications were used for protein identification and quantification: Carbamidomethylation of cysteine residues (+57.021 Da) was set as static modifications, while the oxidation of methionine residues (+15.995 Da), deamidation (+0.984) on asparagine and glutamine were set as a variable modification. Results obtained from MaxQuant. Sequence coverage was obtained with the software Scaffold 5.

Generation of RyR1 mutants and transfection of HEK293 cells

Constructs containing RyR1 mutants were obtained by mutating fragments of rabbit *RYR1* using the QuikChange II XL Site-Directed Mutagenesis Kit (Agilent). Forward primers to introduce the mutations were (mutated codon in parentheses, changed nucleotide in bold),

C3733A: TCATGGCCAAGAGC(**GC**C)CACCTGGAGGAGG, **C3892A**: GATTTCTGCAGCTGCTC(**GA**T)GAGGGGCACAACAACG, **C3973A**: CATCCAGGGCCCC(**GC**C)ACCGGGAACCAG, and **C3892D**: GATTTCTGCAGCTGCTC(**GC**T)GAGGGGCACAACAACG. The reverse primers for each construct were reverse complementary to the primers above. Mutated fragments were subcloned into a full-length rabbit *RYR1* construct in pcDNA3.1 vector using BsiWI and ClaI restriction enzymes, except for C906A where HpaI enzyme was used. Subcloning was confirmed by sequencing. HEK293 cells were grown with Dulbecco's Modified Eagle Medium (DMEM) supplemented with 10% (v/v) fetal bovine serum (Invitrogen), penicillin (100 U/ml), streptomycin (100 µg/ml), and 2 mM L-glutamine in 100-mm dishes for microsomes and in 35-mm glass bottom dishes with 14-mm microwell for fluorescent microscopy. HEK293 cells were transfected with 25 mg per dish of cDNA using PEI MAX (Polysciences) at a 1:5 ratio[68]. Cells were collected or analyzed 48 hours after transfection. To induce oxidation of RyR1 channels, HEK293 cells expressing the mutant RyR1 channels were incubated with H_2O_2 1mM for 30 minutes before washing out with culture media.

Mutant RyR1 microsomes preparation and single channel recordings

Microsomes from HEK293 cells expressing the mutant RyR1 channels were prepared by sonicating cell pellets in lysis buffer [10 mM tris (pH 7.0), 150 mM NaCl, 20 mM NaF, and protease inhibitors (Roche)]. The homogenate was centrifuged at 8000g for 20 min at 4°C, and the resulting supernatant was centrifuged at 37,000g for 40 min at 4°C. The final pellets, containing the microsomes, were resuspended in lysis buffer with addition of 250 mM sucrose, 10 mM Mops (pH 7.4), 10 mM EDTA. Samples were stored at −80°C. Microsomes were fused to planar lipid bilayers formed by painting a lipid mixture of phosphatidylethanolamine and phosphatidylcholine (Avanti Polar Lipids) in a 5:3 ratio in decane across a 200 µm hole in polysulfonate cups (Warner Instruments) separating 2 chambers. The trans chamber (1.0 ml), representing the intra-SR (luminal) compartment, was connected to the head stage input of a bilayer voltage clamp amplifier. The cis chamber (1.0 ml), representing the cytoplasmic

compartment, was held at virtual ground. Asymmetrical solutions used were as follows for the cis solution: 1 mM EGTA, 250/125 mM Hepes/Tris, 50 mM KCl, pH 7.35; and for the trans solution: 53 mM $Ca(OH)_2$, 50 mM KCl, 250 mM Hepes, pH 7.35. Microsomes were added to the cis side and fusion with the lipid bilayer was induced by making the cis side hyperosmotic by the addition of 400-500 mM KCl. After the appearance of potassium and chloride channels, the cis side was perfused with the cis solution. At the end of each experiment, 10 µM ryanodine was added to block and confirm the identity of the RyR1 channels. Single-channel currents were recorded at 0 mV using a Bilayer Clamp BC-525D (Warner Instruments), filtered at 1 kHz using a Low-Pass Bessel Filter 8 Pole (Warner Instruments), and digitized at 4 kHz. All experiments were performed at room temperature (20°C). Data acquisition was performed by using Digidata 1322A and Axoscope 10.1 software (Axon Instruments). The recordings were analyzed using Clampfit 10.1 (Molecular Devices).

Fluorescent microscopy and sarcoplasmic reticulum calcium content determination

Sarcoplasmic reticulum calcium content determination protocol was adapted from Marks lab[69]. For Rycal treatment, cells were incubated overnight with ARM210 (10 µM). HEK293 cells were incubated with 10 µM fluo-4, AM, in culture media for 30 min at 37 °C and then washed out and incubated with Krebs solution (140 mM NaCl, 5 mM KCl, 2 mM $CaCl_2$, 1 mM $MgCl_2$, 11 mM glucose and 5 mM HEPES, pH 7.4). Imaging experiments were performed at room temperature (RT; 26 °C). Caffeine was prepared in Krebs solution and added to the cells at 10 mM. Time-series confocal imaging was performed by excitation with a 488-nm light from the argon laser of a Zeiss LSM 800 inverted confocal microscope (×40 oil immersion lens). Sarcoplasmic reticulum content for each cell was calculated as F/Fo, being F the peak fluorescence after caffeine addition and Fo the 30 second average fluorescence of the cell immediately before caffeine addition. Data were analyzed using ImageJ software and GraphPad Prism.

System preparation for molecular dynamics simulations

Initial systems were built without virtual sites to perform all-atom explicit solvent MD simulations at a 2 fs timestep, referred to as *no-vsites* systems. Two setups were generated, consisting of wild-type and C3892D mutant RyR1 proteins, using the CHARMM-GUI webserver[70]. The starting structure was the wild-type RyR1 co-complexed with cofactors, ATP, caffeine, and Ca^{2+} within the activation core, as well as the drug ARM210 with co-coupled ATP molecules bound in the

RY1&2 domain (PDB: 7TZC)[35]. From this structure, the mutant system was generated by introducing the C3892D mutation across all four protomers using CHARMM-GUI. Both co-complexed proteins were aligned along the z-axis and embedded in a 1-palmitoyl-2-oleoyl-sn-glycero-3-phosphocholine (POPC) bilayer. The systems were solvated with TIP3P water, and 150 mM NaCl was added. The final wild-type and mutant systems contained ~2.47 and ~2.54 million atoms, respectively. A third system lacking ARM210 was derived from the wild-type ARM210-bound setup by removing the drug and the cooperatively bound ATP molecules, followed by manual modification of the coordinate and topology files. Parameters for ATP, ARM210, and caffeine were taken from the CGenFF database[71], while the CHARMM36 force field[72–74] was used for proteins, lipids, water, and ions.

To enable longer integration timesteps, all three systems were further converted into *vsites* systems[75–79] by incorporating virtual sites, allowing a 5 fs timestep. The GROMACS tool pdb2gmx was used to generate virtual hydrogen sites for proteins, lipids, and ligands, while water and ions were left unmodified. The resulting *vsites* systems contained ~2.5 million atoms for the wild-type and ~2.6 million atoms for the mutant construct.

Molecular dynamics simulations

All systems were energy-minimized and equilibrated in seven stages using the CHARMM-GUI standard protocol. The first two stages were carried out in the NVT ensemble, followed by the NPT ensemble in subsequent steps. A v-rescale thermostat[80] and a c-rescale berostat[81] were used to maintain the temperature at 310 K and the pressure at 1 bar, respectively. In the first equilibration stage, harmonic restraints were applied to protein backbone heavy atoms (k = 4000 kJ mol^{-1} nm^{-2}) and side chain (k = 2000 kJ mol^{-1} nm^{-2}) of the protein. For lipids, restraints were applied only to phosphorus atoms (k = 1000 kJ mol^{-1} nm^{-2}). These restraints were gradually released across the equilibration stages. By the final stage, systems reached timesteps of 2 fs (*no-vsites*) or 5 fs (*vsites*). Each system was equilibrated for 100 ns. Unbiased production simulations were then performed under the NVT ensemble at 310 K, with a timestep of 2 fs for *no-vsites* and 5 fs for *vsites* systems. Across all systems and replicates, we achieved a total of 36.6 μs of simulation time (detailed in Table 1). Simulations were performed with GROMACS v2021.4 package[82]. For short-range electrostatics and van der Waals interactions, a cutoff of 12 Å was applied, while long-range electrostatics were treated with the particle-mesh Ewald (PME)

method[83] using a grid size of 1.2 Å. In *no-vsites* systems, hydrogen-containing bonds were constrained, whereas all bonds in the *vsites* systems were constrained using the LINCS algorithm[84]. Simulations were executed on the Chicoma supercomputer at Los Alamos National Laboratory, using 10 computing nodes per run. Each node contained two AMD EPYC 7H12 processors (64 cores each). In total, simulations required ~25 million CPU hours. Trajectory analysis methods are described in the Supplementary Information.

Table 1. Timescales achieved during all-atom explicit solvent MD simulations of the three systems, both with and without virtual sites, i.e. *vsites* and *no-vsites* systems. Integration timesteps are indicated in parentheses.

Integration scheme	Wild type (μs)	Wild type + ARM210 (μs)	C3892d mutant + ARM210 (μs)
no-vsites (2 fs)	3.6	5.0	5.0
vsites (5 fs)	3.6	3.6	3.6
vsites (5 fs)	5.0	3.6	3.6

Acknowledgement

The work was supported by funding from NIH to A.R.M. (5P01HL164319-02, 4R01NS114570-02, 5R01HL140934-08). J. GC was supported from NIH grant T32 HL120826 (to A.R.M.). K.Y.S. and J.D.P. acknowledge generous support from the NIH (NIGMS R35-GM156585) and LANL LDRD 20240384ER. Generous allocations of computational resources on the Chicoma supercomputer by Los Alamos National Laboratory Institutional Computing are gratefully acknowledged. We would like to thank Rajesh Kumar Soni from the Proteomics Shared Resource (HICCC) facility for his essential services.

Author contributions

J.D.P., M.C.M., and J.GC are co-first authors. K.Y.S., J.F., and A.R.M. are corresponding authors. J.D.P., M.C.M., and J.GC designed and interpreted the experiments. J.D.P. and J.GC performed and analyzed the molecular dynamics simulations. M.C.M., H.D., and Q.Y. conducted and analyzed the *in vitro* experiments. A.W., Y.L., and Z.M. contributed to sample preparation. J.D.P. drafted the manuscript with input from M.C.M. and J.GC. All authors reviewed and edited the manuscript. J.D.P., M.C.M., J.GC, K.Y.S., J.F., and A.R.M. conceived the study and directed the overall research. K.Y.S., J.F., and A.R.M. supervised the project and secured funding.

Competing Interest

The authors declare no competing financial interests, except for A.R.M., who owns stock in RyCarma Therapeutics Inc., a company developing compounds targeting RyR.

Data Availability

The datasets generated and/or analyzed during the current study are available from the corresponding authors on request. Source data will be provided with this paper.

References

1. Marks, A. R. *et al.* Molecular cloning and characterization of the ryanodine receptor/junctional channel complex cDNA from skeletal muscle sarcoplasmic reticulum. *Proceedings of the National Academy of Sciences* **86**, 8683–8687 (1989).
2. Flucher, B. E. & Franzini-Armstrong, C. Formation of junctions involved in excitation-contraction coupling in skeletal and cardiac muscle. *Proceedings of the National Academy of Sciences* **93**, 8101–8106 (1996).
3. Franzini-Armstrong, C. & Protasi, F. Ryanodine receptors of striated muscles: a complex channel capable of multiple interactions. *Physiol Rev* **77**, 699–729 (1997).
4. Meissner, G. Ryanodine receptor/Ca^{2+} release channels and their regulation by endogenous effectors. *Annu Rev Physiol* **56**, 485–508 (1994).
5. Van Petegem, F. Ryanodine receptors: structure and function. *Journal of Biological Chemistry* **287**, 31624–31632 (2012).
6. Franzini-Armstrong, C., Protasi, F. & Ramesh, V. Shape, size, and distribution of Ca^{2+} release units and couplons in skeletal and cardiac muscles. *Biophys J* **77**, 1528–1539 (1999).
7. Marx, S. O., Ondrias, K. & Marks, A. R. Coupled gating between individual skeletal muscle Ca^{2+} release channels (ryanodine receptors). *Science (1979)* **281**, 818–821 (1998).
8. Marx, S. O. *et al.* Coupled gating between cardiac calcium release channels (ryanodine receptors). *Circ Res* **88**, 1151–1158 (2001).
9. Porta, M. *et al.* Coupled gating of skeletal muscle ryanodine receptors is modulated by Ca^{2+}, Mg^{2+}, and ATP. *American Journal of Physiology-Cell Physiology* **303**, C682–C697 (2012).
10. Xu, J. *et al.* In situ structural insights into the excitation-contraction coupling mechanism of skeletal muscle. *Sci Adv* **10**, (2024).
11. Fabiato, A. Calcium-induced release of calcium from the cardiac sarcoplasmic reticulum. *J Mol Cell Cardiol* **24**, 28 (1992).
12. Kushmerick, M. J., Moerland, T. S. & Wiseman, R. W. Mammalian skeletal muscle fibers distinguished by contents of phosphocreatine, ATP, and Pi. *Proceedings of the National Academy of Sciences* **89**, 7521–7525 (1992).
13. Nagasaki, K. & Fleischer, S. Ryanodine sensitivity of the calcium release channel of sarcoplasmic reticulum. *Cell Calcium* **9**, 1–7 (1988).
14. Zhang, L., Kelley, J., Schmeisser, G., Kobayashi, Y. M. & Jones, L. R. Complex formation between junctin, triadin, calsequestrin, and the ryanodine receptor. *Journal of Biological Chemistry* **272**, 23389–23397 (1997).
15. Ryan, T. *et al.* Identification of novel ryanodine receptor 1 (RyR1) protein interaction with calcium homeostasis endoplasmic reticulum protein (CHERP). *Journal of Biological Chemistry* **286**, 17060–17068 (2011).

16. Suko, J. *et al.* Phosphorylation of serine 2843 in ryanodine receptor-calcium release channel of skeletal muscle by cAMP-, cGMP- and CaM-dependent protein kinase. *Biochimica et Biophysica Acta (BBA) - Molecular Cell Research* **1175**, 193–206 (1993).
17. Hamilton, S. L. & Reid, M. B. RyR1 modulation by oxidation and calmodulin. *Antioxid Redox Signal* **2**, 41–45 (2000).
18. Brillantes, A.-M. B. *et al.* Stabilization of calcium release channel (ryanodine receptor) function by FK506-binding protein. *Cell* **77**, 513–523 (1994).
19. Kaftan, E., Marks, A. R. & Ehrlich, B. E. Effects of rapamycin on ryanodine receptor/Ca^{2+}-release channels from cardiac muscle. *Circ Res* **78**, 990–997 (1996).
20. Shan, J. *et al.* Role of chronic ryanodine receptor phosphorylation in heart failure and β-adrenergic receptor blockade in mice. *Journal of Clinical Investigation* **120**, 4375–4387 (2010).
21. Marx, S. O. *et al.* PKA phosphorylation dissociates FKBP12.6 from the calcium release channel (ryanodine receptor). *Cell* **101**, 365–376 (2000).
22. Miotto, M. C. *et al.* Structural basis for ryanodine receptor type 2 leak in heart failure and arrhythmogenic disorders. *Nat Commun* **15**, 8080 (2024).
23. Wehrens, X. H. T. *et al.* FKBP12.6 deficiency and defective calcium release channel (ryanodine receptor) function linked to exercise-induced sudden cardiac death. *Cell* **113**, 829–840 (2003).
24. Wehrens, X. H. T. *et al.* Ryanodine receptor/calcium release channel PKA phosphorylation: a critical mediator of heart failure progression. *Proceedings of the National Academy of Sciences* **103**, 511–518 (2006).
25. Bellinger, A. M. *et al.* Hypernitrosylated ryanodine receptor calcium release channels are leaky in dystrophic muscle. *Nat Med* **15**, 325–330 (2009).
26. Kushnir, A. *et al.* Intracellular calcium leak as a therapeutic target for RYR1-related myopathies. *Acta Neuropathol* **139**, 1089–1104 (2020).
27. Lehnart, S. E. *et al.* Sudden death in familial polymorphic ventricular tachycardia associated with calcium release channel (ryanodine receptor) leak. *Circulation* **109**, 3208–3214 (2004).
28. Lehnart, S. E. *et al.* Stabilization of cardiac ryanodine receptor prevents intracellular calcium leak and arrhythmias. *Proceedings of the National Academy of Sciences* **103**, 7906–7910 (2006).
29. Reiken, S. *et al.* β-Blockers restore calcium release channel function and improve cardiac muscle performance in human heart failure. *Circulation* **107**, 2459–2466 (2003).
30. Santulli, G. *et al.* Calcium release channel RyR2 regulates insulin release and glucose homeostasis. *Journal of Clinical Investigation* **125**, 1968–1978 (2015).
31. Dridi, H. *et al.* Role of defective calcium regulation in cardiorespiratory dysfunction in Huntington's disease. *JCI Insight* **5**, (2020).
32. Liu, X. *et al.* Role of leaky neuronal ryanodine receptors in stress-induced cognitive dysfunction. *Cell* **150**, 1055–1067 (2012).
33. Todd, J. J. *et al.* Rycal S48168 (ARM210) for RYR1-related myopathies: a phase one, open-label, dose-escalation trial. *EClinicalMedicine* **68**, 102433 (2024).
34. Steinberg, C. *et al.* RYR2-ryanodinopathies: from calcium overload to calcium deficiency. *Europace* **25**, (2023).
35. Melville, Z. *et al.* A drug and ATP binding site in type 1 ryanodine receptor. *Structure* **30**, 1025-1034.e4 (2022).
36. des Georges, A. *et al.* Structural basis for gating and activation of RyR1. *Cell* **167**, 145-157.e17 (2016).
37. Woll, K. A., Haji-Ghassemi, O. & Van Petegem, F. Pathological conformations of disease mutant ryanodine Receptors revealed by cryo-EM. *Nat Commun* **12**, 807 (2021).

38. Melville, Z., Kim, K., Clarke, O. B. & Marks, A. R. High-resolution structure of the membrane-embedded skeletal muscle ryanodine receptor. *Structure* **30**, 172-180.e3 (2022).
39. Bai, X.-C., Yan, Z., Wu, J., Li, Z. & Yan, N. The central domain of RyR1 is the transducer for long-range allosteric gating of channel opening. *Cell Res* **26**, 995–1006 (2016).
40. Wei, R. *et al.* Structural insights into Ca^{2+}-activated long-range allosteric channel gating of RyR1. *Cell Res* **26**, 977–994 (2016).
41. Nayak, A. R. & Samsó, M. Ca^{2+} inactivation of the mammalian ryanodine receptor type 1 in a lipidic environment revealed by cryo-EM. *Elife* **11**, (2022).
42. Zalk, R. *et al.* Structure of a mammalian ryanodine receptor. *Nature* **517**, 44–49 (2015).
43. Yan, Z. *et al.* Structure of the rabbit ryanodine receptor RyR1 at near-atomic resolution. *Nature* **517**, 50–55 (2015).
44. Efremov, R. G., Leitner, A., Aebersold, R. & Raunser, S. Architecture and conformational switch mechanism of the ryanodine receptor. *Nature* **517**, 39–43 (2015).
45. Miotto, M. C. *et al.* Structural basis for ryanodine receptor type 2 leak in heart failure and arrhythmogenic disorders. *Nat Commun* **15**, 8080 (2024).
46. Miotto, M. C. *et al.* Structural analyses of human ryanodine receptor type 2 channels reveal the mechanisms for sudden cardiac death and treatment. *Sci Adv* **8**, (2022).
47. Chen, Y. S. *et al.* Cryo-EM investigation of ryanodine receptor type 3. *Nat Commun* **15**, 8630 (2024).
48. Cholak, S. *et al.* Allosteric modulation of ryanodine receptor RyR1 by nucleotide derivatives. *Structure* **31**, 790-800.e4 (2023).
49. Zheng, W. & Wen, H. Investigating dual Ca^{2+} modulation of the ryanodine receptor 1 by molecular dynamics simulation. *Proteins: Structure, Function, and Bioinformatics* **88**, 1528–1539 (2020).
50. Greene, D., Barton, M., Luchko, T. & Shiferaw, Y. Molecular dynamics simulations of the cardiac ryanodine receptor type 2 (RyR2) gating mechanism. *J Phys Chem B* **126**, 9790–9809 (2022).
51. Mowrey, D. D. *et al.* Ion-pulling simulations provide insights into the mechanisms of channel opening of the skeletal muscle ryanodine receptor. *Journal of Biological Chemistry* **292**, 12947–12958 (2017).
52. Zhang, A., Yu, H., Liu, C. & Song, C. The Ca^{2+} permeation mechanism of the ryanodine receptor revealed by a multi-site ion model. *Nat Commun* **11**, 922 (2020).
53. Heinz, L. P., Kopec, W., de Groot, B. L. & Fink, R. H. A. In silico assessment of the conduction mechanism of the ryanodine receptor 1 reveals previously unknown exit pathways. *Sci Rep* **8**, 6886 (2018).
54. Schilling, R., Fink, R. H. A. & Fischer, W. B. MD simulations of the central pore of ryanodine receptors and sequence comparison with 2B protein from coxsackie virus. *Biochimica et Biophysica Acta (BBA) - Biomembranes* **1838**, 1122–1131 (2014).
55. Shirvanyants, D. *et al.* Pore dynamics and conductance of RyR1 transmembrane domain. *Biophys J* **106**, 2375–2384 (2014).
56. Yamazawa, T. *et al.* Insights into channel modulation mechanism of RYR1 mutants using Ca^{2+} imaging and molecular dynamics. *Journal of General Physiology* **152**, (2020).
57. Greene, D., Barton, M., Luchko, T. & Shiferaw, Y. Computational analysis of binding interactions between the ryanodine receptor type 2 and calmodulin. *J Phys Chem B* **125**, 10720–10735 (2021).

58. Dulhunty, A., Haarmann, C., Green, D. & Hart, J. How many cysteine residues regulate ryanodine receptor channel activity? *Antioxidants and Redox Signaling* vol. 2 Preprint at https://doi.org/10.1089/ars.2000.2.1-27 (2000).
59. Chirasani, V. R., Pasek, D. A. & Meissner, G. Structural and functional interactions between the Ca^{2+}-, ATP-, and caffeine-binding sites of skeletal muscle ryanodine receptor (RyR1). *Journal of Biological Chemistry* **297**, 101040 (2021).
60. Yuan, Q. *et al.* RyR1-related myopathy mutations in ATP and calcium binding sites impair channel regulation. *Acta Neuropathol Commun* **9**, 186 (2021).
61. Mei, Y. *et al.* Channel gating dependence on pore lining helix glycine residues in skeletal muscle ryanodine receptor. *Journal of Biological Chemistry* **290**, 17535–17545 (2015).
62. Haarmann, C. S., Fink, R. H. A. & Dulhunty, A. F. Oxidation and reduction of pig skeletal muscle ryanodine receptors. *Biophys J* **77**, 3010–3022 (1999).
63. Sun, J., Xu, L., Eu, J. P., Stamler, J. S. & Meissner, G. Classes of thiols that influence the activity of the skeletal muscle calcium release channel. *Journal of Biological Chemistry* **276**, 15625–15630 (2001).
64. Aracena-Parks, P. *et al.* Identification of cysteines involved in S-nitrosylation, S-glutathionylation, and oxidation to disulfides in ryanodine receptor type 1. *Journal of Biological Chemistry* **281**, 40354–40368 (2006).
65. Miotto, M. C. *et al.* Targeting ryanodine receptors with allopurinol and xanthine derivatives for the treatment of cardiac and musculoskeletal weakness disorders. *Proceedings of the National Academy of Sciences* **122**, (2025).
66. Shevchenko, A., Tomas, H., Havli, J., Olsen, J. V & Mann, M. In-gel digestion for mass spectrometric characterization of proteins and proteomes. *Nat Protoc* **1**, 2856–2860 (2006).
67. Meier, F. *et al.* Online parallel accumulation–serial fragmentation (PASEF) with a novel trapped ion mobility mass spectrometer. *Molecular & Cellular Proteomics* **17**, 2534–2545 (2018).
68. Longo, P. A., Kavran, J. M., Kim, M.-S. & Leahy, D. J. Transient mammalian cell transfection with polyethylenimine (PEI). in *Methods in Enzymology* vol. 529 227–240 (2013).
69. Dridi, H. *et al.* Heart failure-induced cognitive dysfunction is mediated by intracellular Ca^{2+} leak through ryanodine receptor type 2. *Nat Neurosci* **26**, 1365–1378 (2023).
70. Lee, J. *et al.* CHARMM-GUI input generator for NAMD, GROMACS, AMBER, OpenMM, and CHARMM/OpenMM simulations using the CHARMM36 additive force field. *J Chem Theory Comput* **12**, 405–413 (2016).
71. Vanommeslaeghe, K. *et al.* CHARMM general force field: a force field for drug-like molecules compatible with the CHARMM all-atom additive biological force fields. *J Comput Chem* **31**, 671–690 (2010).
72. Huang, J. *et al.* CHARMM36m: an improved force field for folded and intrinsically disordered proteins. *Nat Methods* **14**, 71–73 (2017).
73. Klauda, J. B. *et al.* Update of the CHARMM all-atom additive force field for lipids: validation on six lipid types. *J Phys Chem B* **114**, 7830–7843 (2010).
74. MacKerell, A. D., Feig, M. & Brooks, C. L. Improved treatment of the protein backbone in empirical force fields. *J Am Chem Soc* **126**, 698–699 (2004).
75. Feenstra, K. A., Hess, B. & Berendsen, H. J. C. Improving efficiency of large time-scale molecular dynamics simulations of hydrogen-rich systems. *J Comput Chem* **20**, 786–798 (1999).
76. Bjelkmar, P., Larsson, P., Cuendet, M. A., Hess, B. & Lindahl, E. Implementation of the CHARMM force field in GROMACS: analysis of protein stability effects from correction maps, virtual interaction sites, and water models. *J Chem Theory Comput* **6**, 459–466 (2010).

77. Prajapati, J. D., Fernández Solano, C. J., Winterhalter, M. & Kleinekathöfer, U. Characterization of ciprofloxacin permeation pathways across the porin OmpC using metadynamics and a string method. *J Chem Theory Comput* **13**, 4553–4566 (2017).
78. Prajapati, J. D., Solano, C. J. F., Winterhalter, M. & Kleinekathöfer, U. Enrofloxacin permeation pathways across the porin OmpC. *J Phys Chem B* **122**, 1417–1426 (2018).
79. Golla, V. K., Prajapati, J. D., Joshi, M. & Kleinekathöfer, U. Exploration of free energy surfaces across a membrane channel using metadynamics and umbrella sampling. *J Chem Theory Comput* **16**, 2751–2765 (2020).
80. Bussi, G., Donadio, D. & Parrinello, M. Canonical sampling through velocity rescaling. *J Chem Phys* **126**, (2007).
81. Bernetti, M. & Bussi, G. Pressure control using stochastic cell rescaling. *J Chem Phys* **153**, (2020).
82. Abraham, M. J. *et al.* GROMACS: high performance molecular simulations through multi-level parallelism from laptops to supercomputers. *SoftwareX* **1–2**, 19–25 (2015).
83. Essmann, U. *et al.* A smooth particle mesh Ewald method. *J Chem Phys* **103**, 8577–8593 (1995).
84. Hess, B., Bekker, H., Berendsen, H. J. C. & Fraaije, J. G. E. M. LINCS: a linear constraint solver for molecular simulations. *J Comput Chem* **18**, 1463–1472 (1997).

Supplementary Files

This is a list of supplementary files associated with this preprint. Click to download.

- TableS1.xlsx
- RyR1SI.pdf
- RyR1compressed.mov
- RyR1SI.pdf
- FigureS1uncropped.tif
- nrreportingsummary.pdf
- nrsoftwarepolicy.pdf